ACS APPLIED MATERIALS & INTERFACES

www.acsami.org

Research Article

Frequency-Dependent Synapse Weight Tuning in 1S1R with a Short-Term Plasticity TiO_x-Based Exponential Selector

Mun Yin Chee, Putu Andhita Dananjaya, Gerard Joseph Lim, Yuanmin Du, and Wen Siang Lew*

Cite This: *ACS Appl. Mater. Interfaces* 2022, 14, 35959−35968

Read Online

ACCESS | Metrics & More | Article Recommendations | Supporting Information

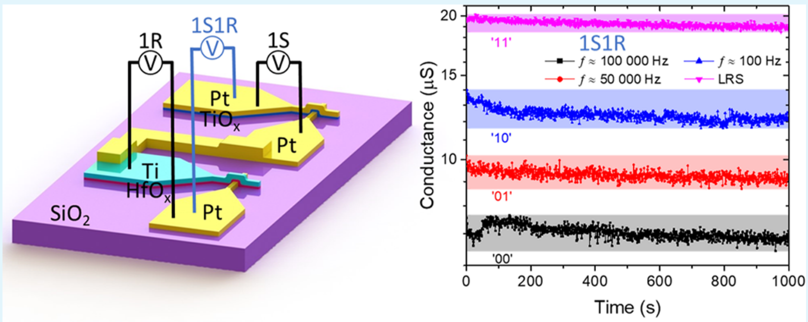

ABSTRACT: Short-term plasticity (STP) is an important synaptic characteristic in the hardware implementation of artificial neural networks (ANN), as it enables the temporal information processing (TIP) capability. However, the STP feature is rather challenging to reproduce from a single nonvolatile resistive random-access memory (RRAM) element, as it requires a certain degree of volatility. In this work, a Pt/TiO_x/Pt exponential selector is introduced not only to suppress the sneak current but also to enable the TIP feature in a one selector-one RRAM (1S1R) synaptic device. Our measurements reveal that the exponential selector exhibits the STP characteristic, while a Pt/HfO_x/Ti RRAM enables the long-term memory capability of the synapse. Thereafter, we experimentally demonstrated pulse frequency-dependent multilevel switching in the 1S1R device, exhibiting the TIP capability of the developed 1S1R synapse. The observed STP of the selector is strongly influenced by the bottom metal−oxide interface, in which Ar plasma treatment on the bottom Pt electrode resulted in the annihilation of the STP feature in the selector. A mechanism is thus proposed to explain the observed STP, using the local electric field enhancement induced at the metal−oxide interface coupled with the drift-diffusion model of mobile O^{2-} and Ti^{3+} ions. This work therefore provides a reliable means of producing the STP feature in a 1S1R device, which demonstrates the TIP capability sought after in hardware-based ANN.

KEYWORDS: *1S1R, short-term plasticity, TiO_x-based selector, RRAM*

■ INTRODUCTION

Hardware realization of artificial neural networks (ANNs) has attracted much attention to demonstrate image classification and pattern recognition tasks.[1−8] In this realization, a memory type that emulates the role of a synapse in neural networks is needed to convey the strength between neurons. Due to the limitation of conventional memories, e.g., volatility of DRAM and high power consumption of FLASH, great efforts have been placed in developing the next generation of nonvolatile memories. Among all of the emerging nonvolatile memories, resistive random-access memory (RRAM), also known as memristor, is the most promising candidate for emulating synapse as it has the multilevel capability,[9−13] low power,[14,15] fast operation,[16,17] and most importantly its great scaling potential in fabrication of large-scale integrated circuits.[18−20] It can achieve a device footprint of $4F^2$ under crossbar array integration, which is suitable for solving complex cognitive tasks that requires a large amount of synapses.

However, the RRAM-based crossbar array faces sneak path current issues as the resistance value of RRAM in the partially selected cells might be small. This sneak current can be suppressed if a selector device is added in series with each RRAM device in the crossbar array.[21−23] The selector should possess a highly nonlinear current−voltage (I−V) characteristic, which blocks current if the applied voltage is low and allows current to flow through with little resistance if the applied voltage is high. With this one selector-one RRAM (1S1R) configuration, the crossbar array can be operated in the V/2 scheme[24,25] or V/3 scheme.[26] Generally, there are two

Received: June 21, 2022
Accepted: July 18, 2022
Published: July 27, 2022

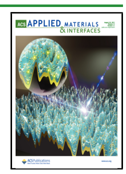

https://doi.org/10.1021/acsami.2c11016
ACS Appl. Mater. Interfaces 2022, 14, 35959−35968

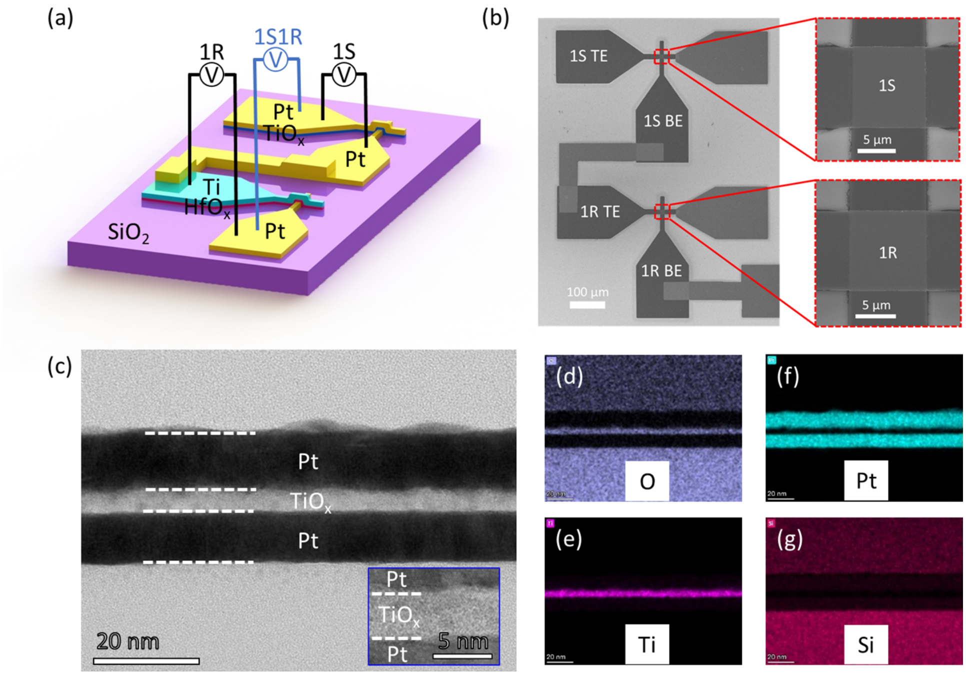

Figure 1. (a) Schematic illustration of the measurement configuration of the standalone 1S, 1R, and the corresponding 1S1R cell. (b) Scanning electron microscopy (SEM) image of the sample with enlarged 10 μm × 10 μm 1S and 1R devices. (c) Cross-sectional high-resolution transmission electron microscopy (HRTEM) image of the Pt/TiO_x/Pt selector. The image reveals that the TiO_x layer thickness is 4 nm. Inset in panel (c) shows the enlarged HRTEM image of the TiO_x film. Elemental distribution EDX maps of (d) O, (e) Ti, (f) Pt, and (g) Si for the Pt/TiO_x/Pt selector.

types of selectors: a threshold type selector and an exponential type selector. In the threshold type selector, the resistance undergoes abrupt transitions between "on" and "off" states at a certain threshold voltage, and the threshold switching mechanism usually involves the formation of an unstable conductive filament.[21,27,28] While in the exponential type selector, the change in the value of resistance with applied voltage is relatively gradual, and the exponential $I-V$ characteristic is usually realized by the thin tunneling barrier oxide layer.[22,29] The exponential type selectors have been shown to maintain the analog property of RRAM due to the slow slope of the $I-V$ curve.[30] Therefore, the exponential selectors are more suitable to be implemented in synapse-like 1S1R.

Synaptic behaviors like spike-timing-dependent plasticity (STDP), long-term potentiation (LTP), long-term depression (LTD), and short-term plasticity (STP) have been demonstrated in RRAM devices.[31−35] In particular, STP has been shown to be suitable to perform temporal information processing (TIP). For instance, STP devices can differentiate and register the stimulation rate in their conductance value.[36−38] However, STP is hard to demonstrate in most RRAMs as it requires volatile switching. Nonetheless, if the selector in 1S1R can demonstrate STP, the 1S1R can perform TIP despite the absence of STP in RRAM. Hence, with this STP selector, RRAM with superior nonvolatile memory performances such as excellent multilevel capability can be chosen without needing to consider STP since the TIP capability is already present in the 1S1R. Therefore, it is of utmost importance to demonstrate STP in an exponential selector; however, such a finding is still elusive.

STP has been shown in TiO_x-based RRAM devices.[39] The resistive switching in TiO_x can be attributed to several mechanisms, for instance, formation and electromigration of oxygen vacancies,[40,41] electromigration of mobile Ti^{3+} cations,[42] migration of Pt atoms via strong metal−support interaction,[43] and transformation to a Magnéli phase Ti_nO_{2n-1}.[44] TiO_x has also been shown to demonstrate a highly nonlinear $I-V$ characteristic, which is desired in the exponential selector.[29,45] However, the STP of TiO_x-based exponential selector has not been reported before.

In this work, we introduce the 1S1R synaptic device based on the Pt/TiO_x/Pt exponential selector and the Pt/HfO_x/Ti RRAM. The Pt/TiO_x/Pt exponential selector is demonstrated to exhibit STP, which enables the TIP capability of the synapse. On the other hand, the memory element comprised of Pt/HfO_x/Ti RRAM structure enables the LTP and LTD capabilities of the synapse. The HfO_x-based RRAM is integrated into the 1S1R as HfO_x-based RRAM has been shown to demonstrate good multilevel states, long retention, and high endurance, and it is also compatible with CMOS processes.[46−50] The 1S1R synaptic capabilities are experimentally demonstrated using different pulse operating modes such as varying pulse frequencies. Plasma treatment on the Pt BE reveals that the bottom Pt/TiO_x interface plays a key role in the STP of the Pt/TiO_x/Pt selector. A mechanism is proposed to explain the observed STP by coupling the local electric field enhancement effect with the drift-diffusion model of mobile Ti^{3+} and O^{2-} ions.

■ EXPERIMENTAL METHODS

Crosspoint structure devices of 10 μm × 10 μm cell area are fabricated by a two-step lithography process for both Pt/TiO_x/Pt selector and Pt/HfO_x/Ti RRAM, as shown in Figure 1a. First, a 10 nm thick Pt bottom electrode (BE) was deposited on a Si/SiO_2 substrate by DC magnetron sputtering deposition. For the selector, a 4 nm thick TiO_x oxide layer was deposited from a TiO_2 ceramic target using 50 W RF magnetron sputtering at 3 mTorr pressure and 20 sccm Ar gas flow. Subsequently, a 10 nm thick Pt top electrode (TE) was deposited by DC magnetron sputtering deposition to form the

https://doi.org/10.1021/acsami.2c11016
ACS Appl. Mater. Interfaces 2022, 14, 35959−35968

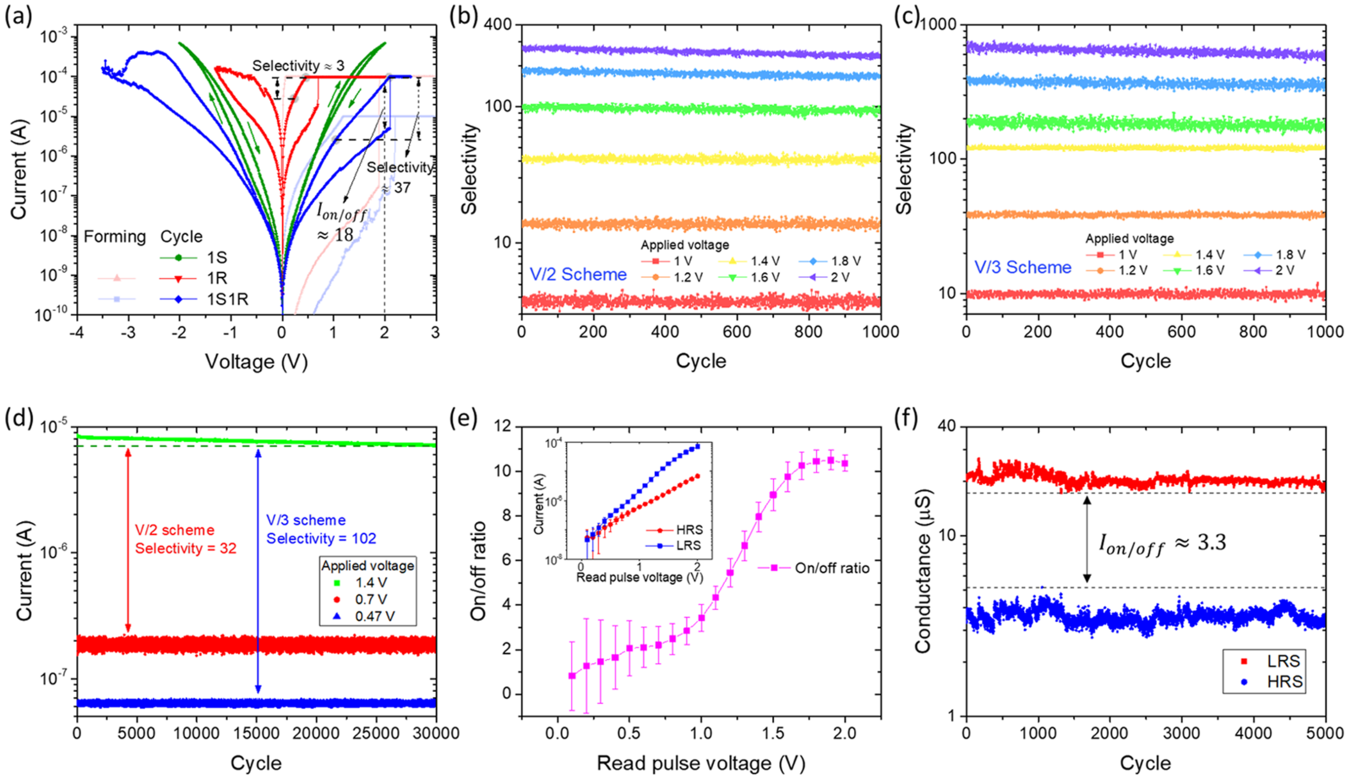

Figure 2. (a) $I-V$ characterization of the standalone Pt/TiO_x/Pt selector, Pt/HfO_x/Ti RRAM, and 1S1R integrated from the selector and RRAM. Selectivity versus cycle of the 1S device under pulse mode for different applied voltages in the (b) V/2 scheme and (c) V/3 scheme. (d) Endurance of the 1S device under 1.4 V applied voltage for the V/2 scheme and V/3 scheme. (e) On/off ratio versus read pulse voltage for 1S1R. The inset in panel (e) shows the current versus read pulse voltage for the HRS and LRS used to calculate the on/off ratio. The error bar is the standard deviation from 100 cycles. (f) Programming endurance of the 1S1R device.

Pt(10 nm)/TiO_x(4 nm)/Pt(10 nm) exponential selector structure. For the RRAM, a 5 nm thick HfO_x switching layer was deposited from a HfO_2 target using 50 W RF magnetron sputtering at 2 mTorr pressure and 20 sccm Ar gas flow. Subsequently, a 50 nm thick Ti TE and a 5 nm Pt passivation layer were deposited to form the Pt(10 nm)/HfO_x(5 nm)/Ti(50 nm) RRAM structure. Finally, a Pt connecting electrode was deposited to connect the selector and the RRAM to form the 1S1R device. This connecting electrode contributes a negligible amount of additional resistance to the 1S1R device as compared to the selector directly stacking on top of the RRAM structure. Through this structure, the selector and the RRAM devices can be characterized and analyzed independently and integrated to form a 1S1R device if required. $I-V$ measurements were conducted using a Keithley 4200A-SCS semiconductor parameter analyzer. The Pt bottom electrodes of the selector or RRAM devices are grounded in the measurements of 1S, 1R, and 1S1R with the combinations, as shown in Figure 1a.

A top view scanning electron microscopy (SEM) image of the 10 μm × 10 μm 1S and 1R devices is shown in Figure 1b. The Pt/TiO_x/Pt selector stack is confirmed by the cross-sectional high-resolution transmission electron microscopy (HRTEM) analysis, as shown in Figure 1c. The thickness of the TiO_x layer is ∼4 nm. The inset of Figure 1c, an enlarged HRTEM image of TiO_x film, shows that the TiO_x film is amorphous, which is further supported by the X-ray diffraction (XRD) analysis, as shown in Figure S1. Figure 1d−g shows the elemental distribution energy-dispersive X-ray spectroscopy (EDX) maps of O, Ti, Pt, and Si, respectively, for the Pt/TiO_x/Pt selector. The maps clearly show the device layer composition and the absence of interdiffusion between the Pt and TiO_x layers.

RESULTS AND DISCUSSION

3.1. 1S, 1R, and 1S1R Synaptic Device Characterizations.

Figure 2a shows the $I-V$ characteristics of the standalone Pt/TiO_x/Pt selector (1S), Pt/HfO_x/Ti RRAM (1R), and the corresponding 1S1R cell from the two. The Pt/TiO_x/Pt exponential selector has a nearly symmetrical $I-V$ curve due to its symmetrical Pt/TiO_x/Pt structure. Furthermore, the Pt/TiO_x/Pt selector exhibits a highly nonlinear IV response with a noticeable hysteresis from the forward−backward sweep. On the other hand, the Pt/HfO_x/Ti RRAM device shows bipolar nonvolatile resistive switching behavior. A positive voltage sweep with a compliance current of 100 μA was applied to form and set the 1R device to LRS. The 1R device has a forming voltage of around 1.9 V and subsequent SET voltages of approximately 0.7 V. In contrast, the 1R device can be reset to HRS at −1.3 V with a gradual reset characteristic, which is favorable in multilevel switching. Upon integration, the 1S1R device has a forming voltage at around 2.2 V and a set voltage at around 2.1 V, and it has an on/off ratio of ∼18 at 2 V reading voltage. Currents of 1S1R for both LRS and HRS are smaller than currents of 1S at all voltages because the 1S and 1R are connected in series in 1S1R, which has a larger resistance than 1S alone. More $I-V$ characterizations of the 1S, 1R, and 1S1R devices are shown in Figure S2. Under the V/2 scheme, the selectivity of the 1S1R, which is 37, is much greater than the selectivity of the 1R device, which is 3. This high selectivity of the 1S1R allows it to be implemented in passive crossbar arrays using the V/2 voltage scheme.

The selectivity of the 1S device was further investigated under pulse mode for different applied voltages in the V/2 scheme and V/3 scheme, as shown in Figure 2b,c, respectively. The pulse width was kept constant at 10 μs for all applied

https://doi.org/10.1021/acsami.2c11016
ACS Appl. Mater. Interfaces 2022, 14, 35959−35968

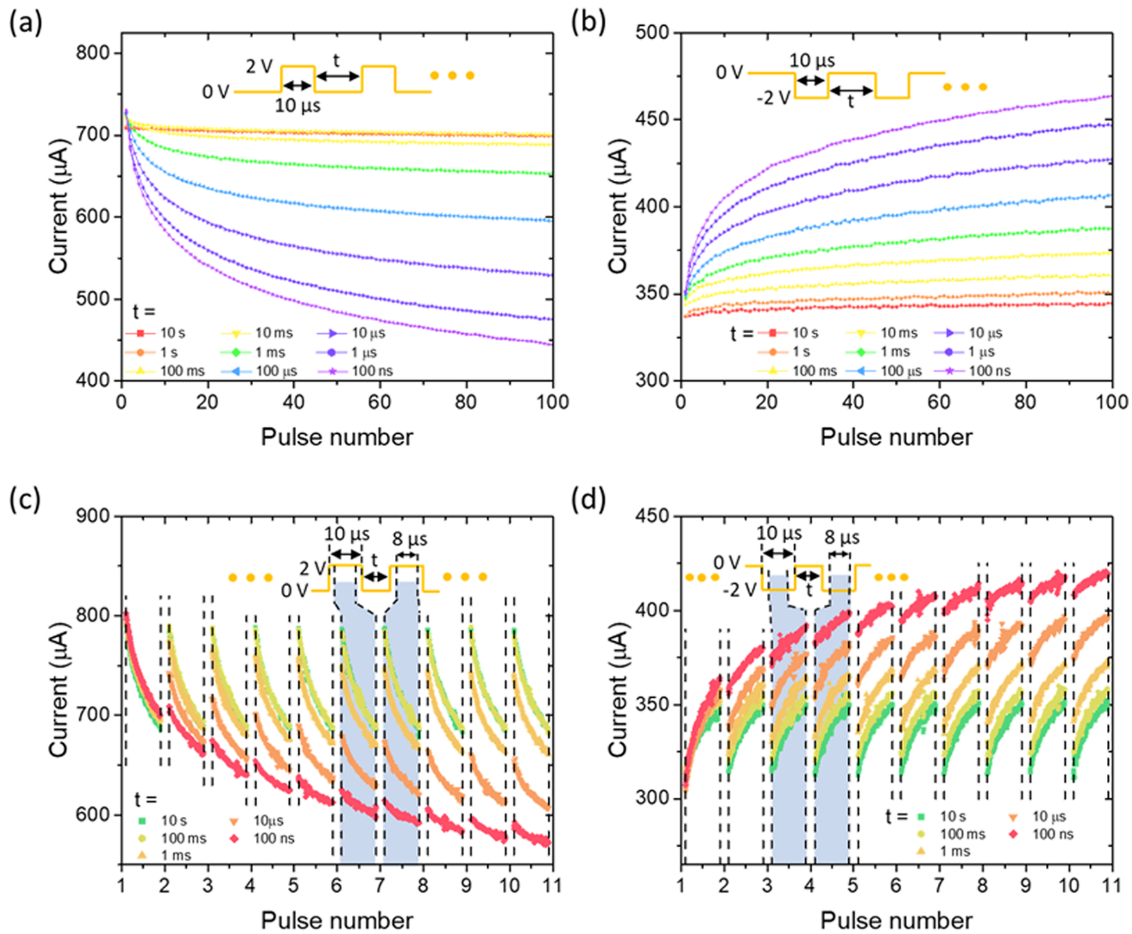

Figure 3. Volatile switching characteristic of Pt/TiO_x/Pt exponential selector under (a) 2 V and (b) −2 V pulses with 10 μs pulse width for various pulse intervals. The measured currents are average from 50 to 75% of the pulses. STP of the Pt/TiO_x/Pt exponential selector under (c) 2 V and (d) −2 V pulses for different pulse intervals. The current waveforms are measured from 10 to 90% portions of the pulses.

voltages. In the V/2 scheme and V/3 scheme, the selectivity increases with applied voltage. For 2 V applied voltage, the selectivities are 218 and 521 in the V/2 scheme and V/3 scheme, respectively. It can be observed that there is a slight degradation in selectivity for high applied voltages (especially 2 and 1.8 V). The current versus cycle measurements of the 1S device for different applied voltages is shown in Figure S3. Under 1.4 V applied voltage, the 1S device can preserve a selectivity of 102 in the V/3 scheme for 30 000 cycles, as shown in Figure 2d.

High read pulse voltages might provide better on/off ratios but, at the same time, create more disturbances to the resistance state. Therefore, it is essential to seek a balance between the on/off ratio and disturbance in the choice of read pulse voltages. To find the optimum read voltage amplitude for 1S1R, the relationship between the on/off ratio of LRS to HRS with read pulse voltage was investigated, as shown in Figure 2e. A 4.4 V and 10 μs pulse set the device from HRS to LRS, and the read pulses have a pulse width of 10 μs. Under a low read voltage regime, the on/off ratios are small with significant variations due to the large variation in low current, as shown in the inset of Figure 2e. The on/off ratio of the 1S1R increases with read pulse voltage until 1.9 V. The decrease in on/off ratio at 2 V is not due to a decrease in LRS current but rather to the larger percentage increase in HRS current than the percentage increase in LRS current. In this study, a 1.4 V read pulse voltage is used in all of the 1S1R measurements because of its adequate on/off ratio and negligible disturbance to the device state.

Figure 2f shows the programming endurance of the 1S1R device under single bipolar pulses. Set pulses of 3.6 V with 10 μs and reset pulses of −4 V with 10 μs were implemented to switch the 1S1R device from HRS to LRS and vice versa. The 1S1R device can maintain an on/off ratio of ∼3.3 for 5000 programming cycles. The standalone 1R device can maintain an on/off ratio of ∼30 for 1000 programming cycles, as shown in Figure S4. This decrease in the on/off ratio for the 1S1R device is attributed to the unchanged resistance of the selector device in the LRS and HRS, which contributes significant resistance to the 1S1R device in the LRS.

Figure 3a,b shows the volatile switching characteristic of the Pt/TiO_x/Pt exponential selector. One hundred pulses at 2 V and 10 μs with varying pulse intervals were applied to the Pt/TiO_x/Pt selector, and the current across the selector was measured. At pulse intervals longer than 1 ms, the currents remain constant throughout the 100 pulses. Whereas at pulse intervals shorter or equal to 1 ms, the currents decrease with pulse number, and these decreases grow with shortening pulse intervals, as shown in Figure 3a. On the other hand, on applying 100 pulses at −2 V and 10 μs, the currents increase with pulse number, which behaves oppositely to the current change in positive 2 V pulses, as shown in Figure 3b. However, these increases grow with decreasing pulse intervals, similar to the behavior in positive 2 V pulses. It should be noted that the

https://doi.org/10.1021/acsami.2c11016
ACS Appl. Mater. Interfaces 2022, 14, 35959−35968

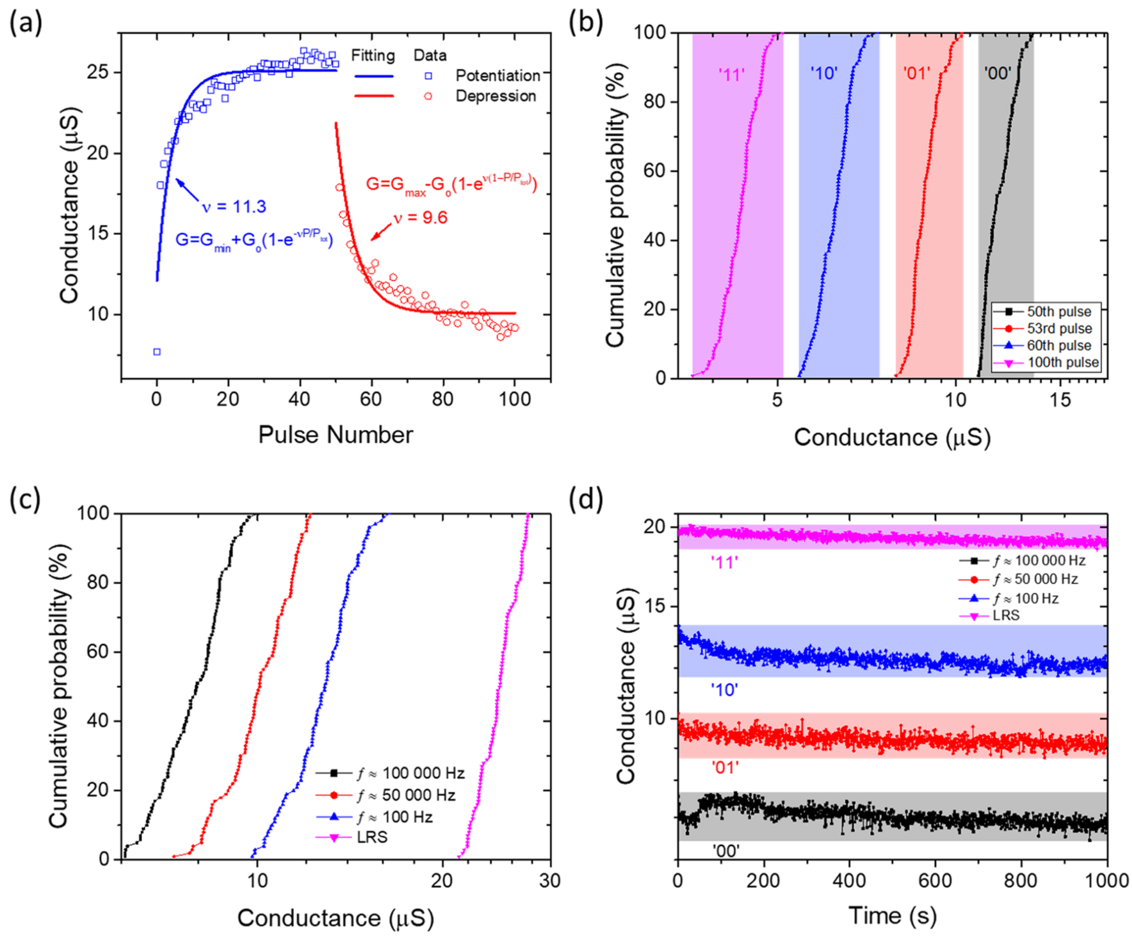

Figure 4. Synapse property of the 1S1R. (a) LTP and LTD performances by the 1S1R treated with fifty 3 V and 10 μs potentiation pulses and fifty −3.4 V and 10 μs depression pulses. (b) Cumulative probability against conductance in 100 cycles for the four multilevel states obtained from the 50th, 53rd, 60th, and 100th pulses in panel (a) but with 3.5 and −3.5 V pulses. Frequency-dependent multilevel switching on the 1S1R. (c) Four multilevel states achieved from an LRS obtained by ten 3.5 V and 10 μs pulses and three HRS obtained by three sets of fifty −3.3 V and 10 μs pulses with different frequencies. (d) Retention characteristic of the four multilevel states in panel (c) with read pulses of 1.4 V and 10 μs.

increases or decreases in current with pulse number are volatile, and the selector device will relax back to the initial state after the pulses are removed. This volatile switching characteristic can explain the nonoverlapping of the forward and backward voltage sweep curves in Figure 2a. Pulses of 2 and −2 V voltages across the Pt/TiO$_x$/Pt selector were investigated as the corresponding currents are around the range of set and reset currents of the 1S1R device, respectively.

Figure 3c,d shows the STP of the Pt/TiO$_x$/Pt exponential selector under 2 and −2 V pulses, respectively. The current waveforms measured from 10 to 90% portions of the pulses were explored. For all pulse intervals, the currents across the selector always decrease whenever a positive voltage pulse is applied, whereas the currents across the selector always increase whenever a negative voltage pulse is applied. It is noted that the selector device can relax back to the initial current state before the next pulse for pulse intervals that are long enough. The relaxations or decays of the conductance are shown in Figure S5. As a result, small current changes with pulse number for long pulse intervals are observed in Figure 3a,b. This pulse frequency-dependent volatile switching characteristic and STP of the exponential selector can be utilized in the 1S1R device to perform TIP, which will be discussed in the next section.

Besides the basic switching of the 1S1R, the synaptic properties of the 1S1R were also investigated, as shown in Figure 4. A set of pulses consisting of 50 potentiation and 50 depression pulses were applied across the 1S1R device, as depicted in Figure 4a. To analyze the LTP and LTD curves, a linearity fitting model was implemented on the conductance change of LTP (G_{LTP}) and LTD (G_{LTD}) as a function of pulse number (P) with the following equations[51,52]

$$G_{LTP} = G_{min} + G_o(1 - e^{-\nu P/P_{tot}}) \quad (1)$$

$$G_{LTD} = G_{max} - G_o(1 - e^{\nu(1-P/P_{tot})}) \quad (2)$$

where G_{min}, G_{max}, G_o, and P_{tot} represent the minimum conductance, the maximum conductance, the change in conductance, and the total pulse number, respectively. ν is the nonlinear parameter extracted from the fitting. The LTD curve is more linear than the LTP curve as the ν value is smaller. This can be ascribed to the gradual reset properties of the Pt/HfO$_x$/Ti RRAM. The LTP and LTD curves of the standalone RRAM device are shown in Figure S7. The 1S1R device shows improvements from the 1R device as the nonlinear parameter ν of the LTD and LTP are smaller in the 1S1R. This result shows that the exponential selector can maintain, if not improve, the linearity of the 1R in the 1S1R synaptic device.[30] Under an optimized number of pulses of 50,

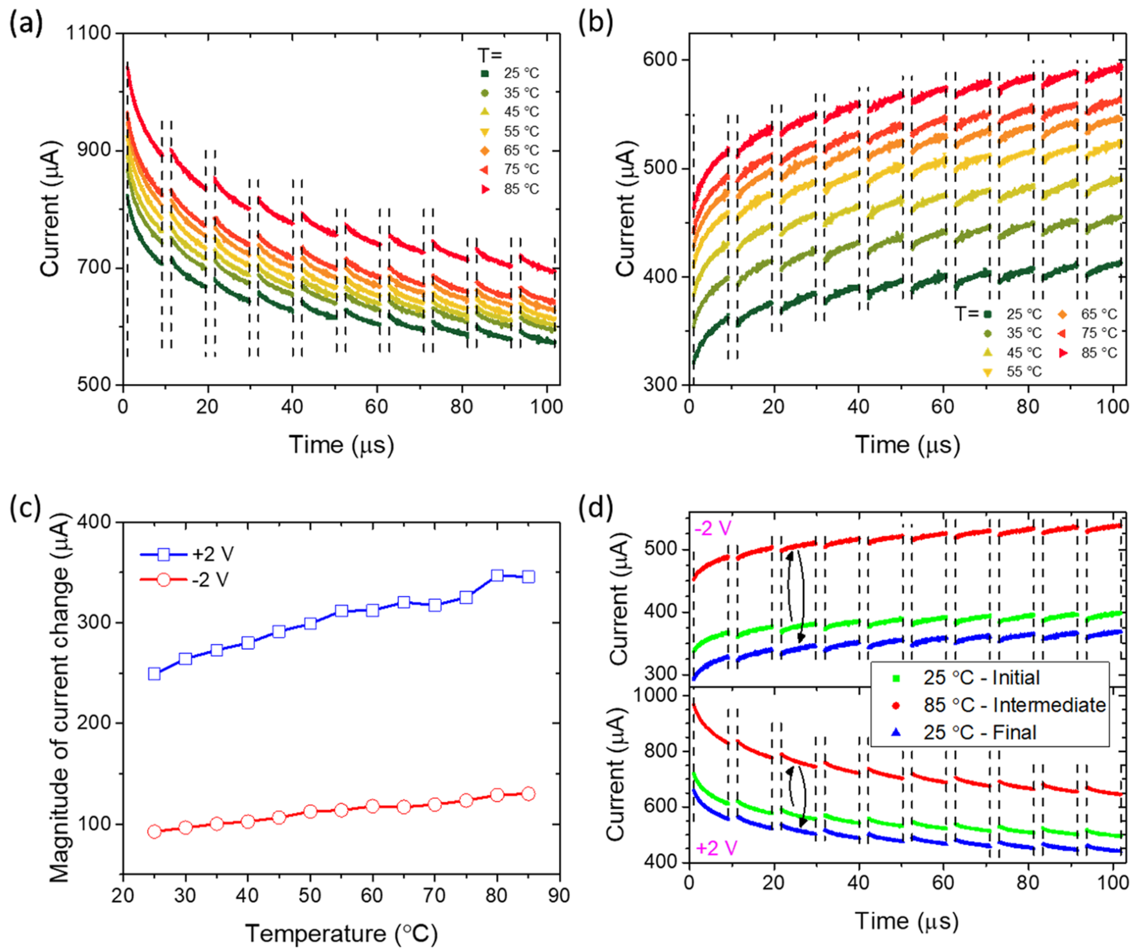

Figure 5. Temperature-dependent measurement on the Pt/TiO_x/Pt exponential selector for (a) 2 V and (b) −2 V pulses with 10 μs pulse width and 100 ns pulse intervals. (c) Magnitude of current change versus temperature for the Pt/TiO_x/Pt exponential selector in panels (a) and (b). (d) Current of the Pt/TiO_x/Pt selector at an initial temperature of 25 °C, heated to 85 °C, and cooled down again to 25 °C for 2 and −2 V pulses.

53, 60, and 100, the 1S1R device can achieve four nonoverlapping multilevel states (2-bit) in 100 cycles, as shown in Figure 4b.

Figure 4c,d shows the frequency-dependent multilevel switching on the 1S1R. This frequency-dependent multilevel switching is not an intrinsic property of the Pt/HfO_x/Ti RRAM as illustrated in Figure S8 but rather is only possible with the STP of the Pt/TiO_x/Pt exponential selector. It utilizes both the increases in the current of the Pt/TiO_x/Pt selector upon applying negative pulses and the decays in the current during the relaxation state, as discussed in Figure 3b,d. On identical negative voltage pulses, the increase in the selector's current is larger for a shorter pulse interval or a higher pulse rate. This higher pulse rate causes the RRAM series connected to the selector to be reset into a higher resistance HRS as the reset current is higher. Frequency-dependent multilevel switching of the 1S1R device was investigated under 50 identical pulses of −3.3 V and 10 μs, as shown in Figure 4c. Three different HRSs and an LRS can be obtained, thus showing the multilevel capability of this programming method, which demonstrates the TIP capability of this 1S1R synaptic device. Figure 4d shows the retention of the four states in Figure 4c. No noticeable drifting of the states was observed for 1000 s.

3.2. Origin of the STP of the Pt/TiO_x/Pt Exponential Selector.

Short-term temporal conductance changes can be associated with the temperature change of the device during operation.[35] As a single voltage pulse is applied across the device, heat is generated by Joule heating throughout the structure. Under multiple pulses operation, this generated heat by one pulse might not be completely dissipated before the arrival of the subsequent pulses within a sufficiently short pulse interval, resulting in the overall increase of device temperature due to the heat accumulation. The device temperature will influence the ionic migration across the oxide layer under the external electric field. Thus, to investigate the origin of STP in the Pt/TiO_x/Pt exponential selector, a temperature-dependent study was carried out under 2 and −2 V pulses with 10 μs pulse width and 100 ns pulse intervals, as shown in Figure 5a,b, respectively. Under the same temperature, the device current decreases with pulses of 2 V and 10 μs, whereas the device current increases with pulses of −2 V and 10 μs. This suggests that there is a possible difference between the bottom and top electrode−oxide interfaces despite having a seemingly symmetrical structure. On the other hand, the device current increases for both pulse polarities as the temperature increases from 25 to 85 °C. This result reveals that the STP of the Pt/TiO_x/Pt selector is not primarily due to the elevated device temperature as the device current increases with temperature for both pulse polarities but decreases with 2 V pulses. Furthermore, the total current change of the device from its initial state increases with temperature, as depicted in Figure

https://doi.org/10.1021/acsami.2c11016
ACS Appl. Mater. Interfaces 2022, 14, 35959−35968

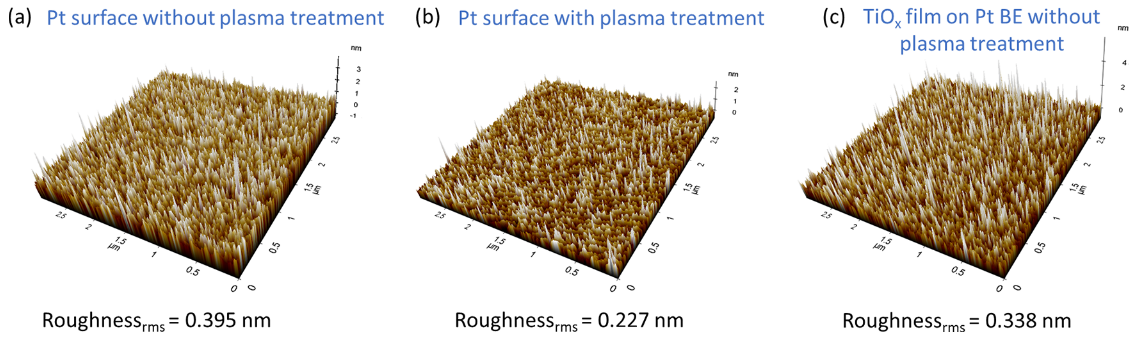

Figure 6. Atomic force microscopy (AFM) topographic images of the Pt BE surface (a) without plasma treatment and (b) with plasma treatment, and (c) TiO_x film on Pt BE without plasma treatment.

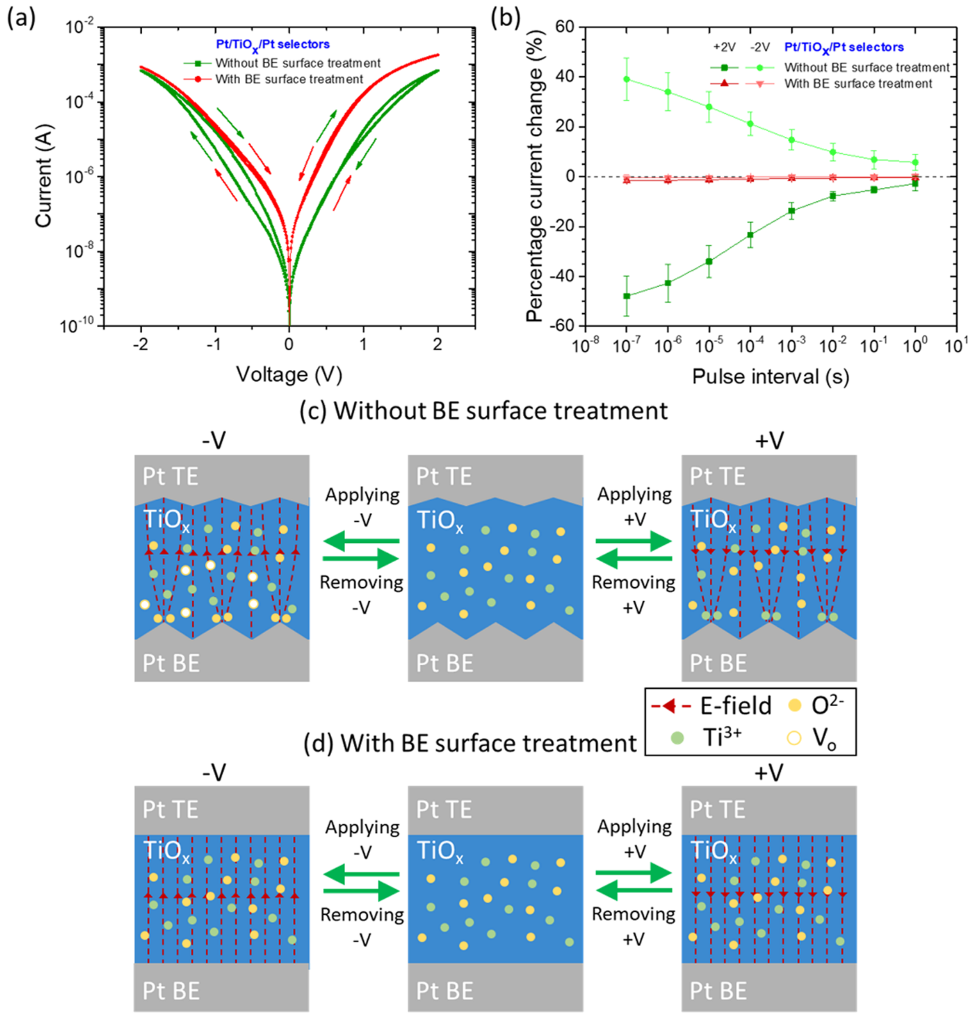

Figure 7. (a) *I*−*V* characterization of the Pt/TiO_x/Pt selector devices with and without the Pt BE surface plasma treatment. (b) Volatile switching characteristics of the Pt/TiO_x/Pt selector devices with and without Pt BE surface plasma treatment for one hundred 2 or −2 V pulses with eight different pulse intervals. The volatile switching characteristic of the Pt/TiO_x/Pt selector device without the surface treatment is also shown in Figure 3. The proposed volatile switching mechanisms of the Pt/TiO_x/Pt selector devices (c) without BE surface treatment and (d) with BE surface treatment.

5c. This data supports the importance of the Joule heating effect to the STP characteristic in the Pt/TiO_x/Pt selector. Figure 5d shows the current of the Pt/TiO_x/Pt selector at an initial temperature of 25 °C, heated to 85 °C, and cooled down again to 25 °C for 2 and −2 V pulses. The current of the selector decreases from the initial 25 °C to the final 25 °C. This current decrease by thermal stress has a similar trend to the current decrease by the excessive number of applied voltage pulses in Figure 2b−d, indicating that the slight degradation in selectivity could be ascribed to the thermal stress by the Joule heating effect.

To further investigate the effect of the electrode−oxide interface, plasma treatment was performed on the BE Pt surface before the second step lithography process. The surface

https://doi.org/10.1021/acsami.2c11016
ACS Appl. Mater. Interfaces 2022, 14, 35959−35968

treatment employs Ar plasma with 25 W power, 3 mTorr pressure, and 45 sccm Ar gas flow for 1 min. This process aims to induce changes in Pt BE surface topography under Ar ion bombardment, which also results in approximately 1 nm etching of the Pt BE surface. The atomic force microscopy (AFM) topographic images of Pt BE surface without and with plasma treatment are shown in Figure 6a,b, respectively. The Pt BE surface becomes smoother after the plasma treatment because some of the protruding parts were etched and removed in the plasma treatment process. The root-mean-square (RMS) roughness and peak-to-valley height of the Pt BE surface are reduced from 0.395 and 5.387 nm to 0.227 and 3.350 nm, respectively. The TiO_x film on Pt BE without plasma treatment exhibits a lower RMS roughness (0.338 nm) than the Pt BE itself (0.395 nm), as shown in Figure 6c. The lower surface roughness could be attributed to the lower sputtering deposition rate of the TiO_x (0.0023 nm/s) than the Pt (0.067 nm/s), which provides sufficient time for surface diffusion of adatoms during the growth process.[53]

Figure 7a shows the $I-V$ characterization of the Pt/TiO_x/Pt selector devices without Pt BE surface plasma treatment (device 1) and with Pt BE surface plasma treatment (device 2). The $I-V$ hysteresis loop for device 2 is much smaller than device 1, indicating much lesser or no volatile switching behavior in device 2. In the negative voltage region, the $I-V$ hysteresis loops show the same clockwise direction for both devices, while in the positive voltage region, the $I-V$ hysteresis loops show opposite directions (clockwise for device 1 and anticlockwise for device 2). The negligible $I-V$ hysteresis characteristic of device 2 could be attributed to the increase in current due to the Joule heating effect under positive or negative voltages sweeps. Figure 7b shows the volatile switching characteristics of device 1 and device 2 for one hundred 2 or −2 V pulses with different pulse intervals. The percentage current change is calculated from the average value of 15 devices from the three batches of samples, as shown in Figure S9 and the error bar is the standard deviation. The percentage current change of device 2 is negligible across all pulse intervals as compared to device 1. This result indicates that the STP is absent in the Pt/TiO_x/Pt selector device with surface plasma treatment. Therefore, the rough BE Pt/TiO_x interface, which induces a local electric field enhancement in the TiO_x layer,[54−56] is necessary for the STP of the Pt/TiO_x/Pt exponential selector.

It is known that the electromigration of mobile O^{2-} and Ti^{3+} ions can induce the resistive switching behavior in TiO_x-based devices.[40−42] The observed STP characteristic of the Pt/TiO_x/Pt exponential selector can be explained using the local electric field enhancement induced at the electrode−oxide interface, coupled with the drift-diffusion model of mobile O^{2-} and Ti^{3+} ions. The plausible STP or volatile switching mechanism of the Pt/TiO_x/Pt exponential selector is illustrated in Figure 7c,d for device 1 and device 2, respectively. When a positive voltage bias is applied on the TE, the Ti^{3+} cations drift to the BE Pt/TiO_x interface in device 1 due to the sufficiently large concentrated electric field; on the other hand, there is less migration of mobile ions in device 2 due to the uniform electric field produced by smoother interfaces. As a result, the number of conductive Ti^{3+} cations decreases in the TiO_x bulk for device 1, which causes the current to decrease. When the positive voltage bias is removed, the Ti^{3+} cations diffuse back to the initial position due to the concentration gradient, and the current relaxes back to the initial value after a sufficiently long duration. When a negative voltage bias is applied on the TE, the O^{2-} anions in device 1 drift to the BE Pt/TiO_x interface, leaving behind oxygen vacancies, whereas there is less migration of anions in device 2. As a result, the number of oxygen vacancies in device 1 increases, which causes the current to increase. It is important to note that the Ti^{3+} cations are not drifting significantly to the TE interface as the RMS roughness is lower for TiO_x film at the TE interface. When the negative voltage bias is removed, the O^{2-} anions diffuse back and recombine with the oxygen vacancies, and the current relaxes back to the initial value after a sufficiently long duration. These microscopic processes explain the STP or volatile switching mechanism of the Pt/TiO_x/Pt exponential selectors, as observed in the experiment.

■ CONCLUSIONS

In summary, we developed a 1S1R synaptic device that consists of an STP Pt/TiO_x/Pt exponential selector and a Pt/HfO_x/Ti RRAM. Its underlying memory device performance followed by the desired synaptic device properties, i.e., analog potentiation−depression and pulse frequency-dependent multilevel switching, have been characterized. The pulse frequency or stimulation rate-dependent multilevel switching characteristic, originated from the STP of the Pt/TiO_x/Pt exponential selector, exhibits the TIP capability of the synapse. Temperature-dependent measurements on the exponential selector device reveal that the elevated temperature of the device by Joule heating is not the primary cause of the STP. A Pt/TiO_x/Pt exponential selector with a smooth BE Pt/TiO_x interface was fabricated by utilizing plasma treatment on the Pt BE surface. Our measurements reveal that the rough BE Pt/TiO_x interface, which induces a local electric field enhancement in the TiO_x layer, is crucial for the STP of the Pt/TiO_x/Pt exponential selector. A plausible STP or volatile switching mechanism of the Pt/TiO_x/Pt exponential selector has been proposed by coupling the local electric field enhancement effect with the drift-diffusion model of mobile Ti^{3+} and O^{2-} ions. Even though the above 1S1R device demonstrated frequency-dependent synapse weight tuning, the on/off ratio of the device is still relatively small (∼18). However, this small on/off ratio can be overcome by choosing an RRAM device with a high on/off ratio while retaining the STP Pt/TiO_x/Pt exponential selector. This study thus provides an alternative way to further the TIP capability in hardware-based ANN based on 1S1R.

■ ASSOCIATED CONTENT

Supporting Information

The Supporting Information is available free of charge at https://pubs.acs.org/doi/10.1021/acsami.2c11016.

XRD patterns of Pt(10 nm)/TiO_x(20 nm) film and TiO_x(20 nm) film (Figure S1); $I-V$ characterization of the standalone 1S, 1R, and 1S1R integrated from the 1S and 1R (Figure S2); current versus cycle of the Pt/TiO_x/Pt selector with different applied pulse voltages (Figure S3); resistive switching of the Pt/HfO_x/Ti RRAM under single bipolar pulses (Figure S4); relaxation of conductance of the STP Pt/TiO_x/Pt exponential selector (Figure S5); current of the Pt/TiO_x/Pt exponential selector under 1 and −1 V pulses (Figure S6); LTP and LTD performances by the Pt/HfO_x/Ti RRAM device (Figure S7); frequency-depend-

https://doi.org/10.1021/acsami.2c11016
ACS Appl. Mater. Interfaces 2022, 14, 35959−35968

ent multilevel switching performed on the Pt/HfO_x/Ti RRAM alone (Figure S8); and volatile switching characteristics of the Pt/TiO_x/Pt selector devices without and with Pt BE surface plasma treatment for three different batches of samples (Figure S9) (PDF)

AUTHOR INFORMATION

Corresponding Author

Wen Siang Lew − *School of Physical and Mathematical Sciences, Nanyang Technological University, Singapore 637371, Singapore;* orcid.org/0000-0002-5161-741X; Email: wensiang@ntu.edu.sg

Authors

Mun Yin Chee − *School of Physical and Mathematical Sciences, Nanyang Technological University, Singapore 637371, Singapore;* orcid.org/0000-0002-1580-1463

Putu Andhita Dananjaya − *School of Physical and Mathematical Sciences, Nanyang Technological University, Singapore 637371, Singapore;* orcid.org/0000-0001-9416-6455

Gerard Joseph Lim − *School of Physical and Mathematical Sciences, Nanyang Technological University, Singapore 637371, Singapore;* orcid.org/0000-0003-2411-5841

Yuanmin Du − *School of Physical and Mathematical Sciences, Nanyang Technological University, Singapore 637371, Singapore*

Complete contact information is available at: https://pubs.acs.org/10.1021/acsami.2c11016

Notes

The authors declare no competing financial interest.

ACKNOWLEDGMENTS

This work was supported by a RIE2020 ASTAR AME IAF-ICP Grant (No. I1801E0030).

REFERENCES

(1) Li, X.; Tang, J.; Zhang, Q.; Gao, B.; Yang, J. J.; Song, S.; Wu, W.; Zhang, W.; Yao, P.; Deng, N.; Deng, L.; Xie, Y.; Qian, H.; Wu, H. Power-Efficient Neural Network with Artificial Dendrites. *Nat. Nanotechnol.* **2020**, *15*, 776−782.

(2) Ambrogio, S.; Narayanan, P.; Tsai, H.; Shelby, R. M.; Boybat, I.; di Nolfo, C.; Sidler, S.; Giordano, M.; Bodini, M.; Farinha, N. C. P.; Killeen, B.; Cheng, C.; Jaoudi, Y.; Burr, G. W. Equivalent-Accuracy Accelerated Neural-Network Training Using Analogue Memory. *Nature* **2018**, *558*, 60−67.

(3) Shulaker, M. M.; Hills, G.; Park, R. S.; Howe, R. T.; Saraswat, K.; Wong, H.-S. P.; Mitra, S. Three-Dimensional Integration of Nanotechnologies for Computing and Data Storage on a Single Chip. *Nature* **2017**, *547*, 74−78.

(4) Yao, P.; Wu, H.; Gao, B.; Eryilmaz, S. B.; Huang, X.; Zhang, W.; Zhang, Q.; Deng, N.; Shi, L.; Wong, H.-S. P.; Qian, H. Face Classification Using Electronic Synapses. *Nat. Commun.* **2017**, *8*, No. 15199.

(5) Sheridan, P. M.; Cai, F.; Du, C.; Ma, W.; Zhang, Z.; Lu, W. D. Sparse Coding with Memristor Networks. *Nat. Nanotechnol.* **2017**, *12*, 784−789.

(6) Li, C.; Belkin, D.; Li, Y.; Yan, P.; Hu, M.; Ge, N.; Jiang, H.; Montgomery, E.; Lin, P.; Wang, Z.; Song, W.; Strachan, J. P.; Barnell, M.; Wu, Q.; Williams, R. S.; Yang, J. J.; Xia, Q. Efficient and Self-Adaptive in-Situ Learning in Multilayer Memristor Neural Networks. *Nat. Commun.* **2018**, *9*, No. 2385.

(7) Li, Y.; Loh, L.; Li, S.; Chen, L.; Li, B.; Bosman, M.; Ang, K.-W. Anomalous Resistive Switching in Memristors Based on Two-Dimensional Palladium Diselenide Using Heterophase Grain Boundaries. *Nat. Electron.* **2021**, *4*, 348−356.

(8) Prezioso, M.; Merrikh-Bayat, F.; Hoskins, B. D.; Adam, G. C.; Likharev, K. K.; Strukov, D. B. Training and Operation of an Integrated Neuromorphic Network Based on Metal-Oxide Memristors. *Nature* **2015**, *521*, 61−64.

(9) Lee, T. S.; Lee, N. J.; Abbas, H.; Lee, H. H.; Yoon, T.-S.; Kang, C. J. Compliance Current-Controlled Conducting Filament Formation in Tantalum Oxide-Based RRAM Devices with Different Top Electrodes. *ACS Appl. Electron. Mater.* **2020**, *2*, 1154−1161.

(10) Ding, G.; Wang, Y.; Zhang, G.; Zhou, K.; Zeng, K.; Li, Z.; Zhou, Y.; Zhang, C.; Chen, X.; Han, S.-T. 2D Metal−Organic Framework Nanosheets with Time-Dependent and Multilevel Memristive Switching. *Adv. Funct. Mater.* **2019**, *29*, No. 1806637.

(11) He, C.; Shi, Z.; Zhang, L.; Yang, W.; Yang, R.; Shi, D.; Zhang, G. Multilevel Resistive Switching in Planar Graphene/SiO_2 Nanogap Structures. *ACS Nano* **2012**, *6*, 4214−4221.

(12) Hwang, S. K.; Lee, J. M.; Kim, S.; Park, J. S.; Park, H. I.; Ahn, C. W.; Lee, K. J.; Lee, T.; Kim, S. O. Flexible Multilevel Resistive Memory with Controlled Charge Trap B- and N-Doped Carbon Nanotubes. *Nano Lett.* **2012**, *12*, 2217−2221.

(13) Stathopoulos, S.; Khiat, A.; Trapatseli, M.; Cortese, S.; Serb, A.; Valov, I.; Prodromakis, T. Multibit Memory Operation of Metal-Oxide Bi-Layer Memristors. *Sci. Rep.* **2017**, *7*, No. 17532.

(14) Yu, S.; Gao, B.; Fang, Z.; Yu, H.; Kang, J.; Wong, H.-S. P. A Low Energy Oxide-Based Electronic Synaptic Device for Neuromorphic Visual Systems with Tolerance to Device Variation. *Adv. Mater.* **2013**, *25*, 1774−1779.

(15) Kim, Y.; Choi, H.; Park, H. S.; Kang, M. S.; Shin, K.-Y.; Lee, S.-S.; Park, J. H. Reliable Multistate Data Storage with Low Power Consumption by Selective Oxidation of Pyramid-Structured Resistive Memory. *ACS Appl. Mater. Interfaces* **2017**, *9*, 38643−38650.

(16) Chen, Z.; Huang, W.; Zhao, W.; Hou, C.; Ma, C.; Liu, C.; Sun, H.; Yin, Y.; Li, X. Ultrafast Multilevel Switching in Au/YIG/n-Si RRAM. *Adv. Electron. Mater.* **2019**, *5*, No. 1800418.

(17) Nagareddy, V. K.; Barnes, M. D.; Zipoli, F.; Lai, K. T.; Alexeev, A. M.; Craciun, M. F.; Wright, C. D. Multilevel Ultrafast Flexible Nanoscale Nonvolatile Hybrid Graphene Oxide−Titanium Oxide Memories. *ACS Nano* **2017**, *11*, 3010−3021.

(18) Al-Haddad, A.; Wang, C.; Qi, H.; Grote, F.; Wen, L.; Bernhard, J.; Vellacheri, R.; Tarish, S.; Nabi, G.; Kaiser, U.; Lei, Y. Highly-Ordered 3D Vertical Resistive Switching Memory Arrays with Ultralow Power Consumption and Ultrahigh Density. *ACS Appl. Mater. Interfaces* **2016**, *8*, 23348−23355.

(19) Chen, Q.; Wang, Z.; Lin, M.; Qi, X.; Yu, Z.; Wu, L.; Bao, L.; Ling, Y.; Qin, Y.; Cai, Y.; Huang, R. Homogeneous 3D Vertical Integration of Parylene-C Based Organic Flexible Resistive Memory on Standard CMOS Platform. *Adv. Electron. Mater.* **2021**, *7*, No. 2000864.

(20) Sokolov, A. S.; Jeon, Y. R.; Kim, S.; Ku, B.; Choi, C. Bio-Realistic Synaptic Characteristics in the Cone-Shaped ZnO Memristive Device. *NPG Asia Mater.* **2019**, *11*, No. 5.

(21) Dananjaya, P. A.; Loy, D. J. J.; Chow, S. C. W.; Lew, W. S. Unidirectional Threshold Switching Induced by Cu Migration with High Selectivity and Ultralow OFF Current under Gradual Electroforming Treatment. *ACS Appl. Electron. Mater.* **2019**, *1*, 2076−2085.

(22) Lee, W.; Park, J.; Kim, S.; Woo, J.; Shin, J.; Choi, G.; Park, S.; Lee, D.; Cha, E.; Lee, B. H.; Hwang, H. High Current Density and Nonlinearity Combination of Selection Device Based on TaO_x/TiO_2/TaO_x Structure for One Selector−One Resistor Arrays. *ACS Nano* **2012**, *6*, 8166−8172.

(23) Lashkare, S.; Panwar, N.; Kumbhare, P.; Das, B.; Ganguly, U. PCMO-Based RRAM and NPN Bipolar Selector as Synapse for Energy Efficient STDP. *IEEE Electron Device Lett.* **2017**, *38*, 1212−1215.

(24) Chen, Y.-C.; Lin, C.-C.; Chang, Y.-F. Post-Moore Memory Technology: Sneak Path Current (SPC) Phenomena on RRAM Crossbar Array and Solutions. *Micromachines* **2021**, *12*, 50.

(25) Zhuo, V. Y.; Chen, Z.; Chui, K. J. *Resistive Random Access Memory Device Physics and Array Architectures BT - Emerging Non-Volatile Memory Technologies: Physics, Engineering, and Applications*, Lew, W. S.; Lim, G. J.; Dananjaya, P. A., Eds.; Springer Singapore: Singapore, 2021; pp 319−343.

(26) Yu, S. Resistive Random Access Memory (RRAM). *Synth. Lect. Emerging Eng. Technol.* **2016**, *2*, 1−79.

(27) Wang, Z.; Rao, M.; Midya, R.; Joshi, S.; Jiang, H.; Lin, P.; Song, W.; Asapu, S.; Zhuo, Y.; Li, C.; Wu, H.; Xia, Q.; Yang, J. J. Threshold Switching of Ag or Cu in Dielectrics: Materials, Mechanism, and Applications. *Adv. Funct. Mater.* **2018**, *28*, No. 1704862.

(28) Peng, H. Y.; Li, Y. F.; Lin, W. N.; Wang, Y. Z.; Gao, X. Y.; Wu, T. Deterministic Conversion between Memory and Threshold Resistive Switching via Tuning the Strong Electron Correlation. *Sci. Rep.* **2012**, *2*, No. 442.

(29) Lee, S.; Woo, J.; Lee, D.; Cha, E.; Hwang, H. Internal Resistor of Multi-Functional Tunnel Barrier for Selectivity and Switching Uniformity in Resistive Random Access Memory. *Nanoscale Res. Lett.* **2014**, *9*, No. 364.

(30) Woo, J.; Yu, S. Impact of Selector Devices in Analog RRAM-Based Crossbar Arrays for Inference and Training of Neuromorphic System. *IEEE Trans. VLSI Syst.* **2019**, *27*, 2205−2212.

(31) Li, T.; Yu, H.; Chen, S. H. Y.; Zhou, Y.; Han, S.-T. The Strategies of Filament Control for Improving the Resistive Switching Performance. *J. Mater. Chem. C* **2020**, *8*, 16295−16317.

(32) Gao, L.; Ren, Q.; Sun, J.; Han, S.-T.; Zhou, Y. Memristor Modeling: Challenges in Theories, Simulations, and Device Variability. *J. Mater. Chem. C* **2021**, *9*, 16859−16884.

(33) Yan, X.; Zhao, J.; Liu, S.; Zhou, Z.; Liu, Q.; Chen, J.; Liu, X. Y. Memristor with Ag-Cluster-Doped TiO_2 Films as Artificial Synapse for Neuroinspired Computing. *Adv. Funct. Mater.* **2018**, *28*, No. 1705320.

(34) Chang, T.; Jo, S. H.; Lu, W. Short-Term Memory to Long-Term Memory Transition in a Nanoscale Memristor. *ACS Nano* **2011**, *5*, 7669−7676.

(35) Kim, S.; Du, C.; Sheridan, P.; Ma, W.; Choi, S.; Lu, W. D. Experimental Demonstration of a Second-Order Memristor and Its Ability to Biorealistically Implement Synaptic Plasticity. *Nano Lett.* **2015**, *15*, 2203−2211.

(36) Lee, Y.; Mahata, C.; Kang, M.; Kim, S. Short-Term and Long-Term Synaptic Plasticity in $Ag/HfO_2/SiO_2/Si$ Stack by Controlling Conducting Filament Strength. *Appl. Surf. Sci.* **2021**, *565*, No. 150563.

(37) Ohno, T.; Hasegawa, T.; Tsuruoka, T.; Terabe, K.; Gimzewski, J. K.; Aono, M. Short-Term Plasticity and Long-Term Potentiation Mimicked in Single Inorganic Synapses. *Nat. Mater.* **2011**, *10*, 591−595.

(38) Cho, H.; Kim, S. Enhancing Short-Term Plasticity by Inserting a Thin TiO_2 Layer in WO_x-Based Resistive Switching Memory. *Coatings* **2020**, *10*, 908.

(39) Berdan, R.; Vasilaki, E.; Khiat, A.; Indiveri, G.; Serb, A.; Prodromakis, T. Emulating Short-Term Synaptic Dynamics with Memristive Devices. *Sci. Rep.* **2016**, *6*, No. 18639.

(40) Jameson, J. R.; Fukuzumi, Y.; Wang, Z.; Griffin, P.; Tsunoda, K.; Meijer, G. I.; Nishi, Y. Field-Programmable Rectification in Rutile TiO_2 Crystals. *Appl. Phys. Lett.* **2007**, *91*, No. 112101.

(41) Illarionov, G. A.; Morozova, S. M.; Chrishtop, V. V.; Einarsrud, M.-A.; Morozov, M. I. Memristive TiO(2): Synthesis, Technologies, and Applications. *Front. Chem.* **2020**, *8*, No. 724.

(42) Carta, D.; Salaoru, I.; Khiat, A.; Regoutz, A.; Mitterbauer, C.; Harrison, N. M.; Prodromakis, T. Investigation of the Switching Mechanism in TiO_2-Based RRAM: A Two-Dimensional EDX Approach. *ACS Appl. Mater. Interfaces* **2016**, *8*, 19605−19611.

(43) Jang, M. H.; Agarwal, R.; Nukala, P.; Choi, D.; Johnson, A. T. C.; Chen, I.-W.; Agarwal, R. Observing Oxygen Vacancy Driven Electroforming in Pt−TiO_2−Pt Device via Strong Metal Support Interaction. *Nano Lett.* **2016**, *16*, 2139−2144.

(44) Kwon, D.-H.; Kim, K. M.; Jang, J. H.; Jeon, J. M.; Lee, M. H.; Kim, G. H.; Li, X.-S.; Park, G.-S.; Lee, B.; Han, S.; Kim, M.; Hwang, C. S. Atomic Structure of Conducting Nanofilaments in TiO_2 Resistive Switching Memory. *Nat. Nanotechnol.* **2010**, *5*, 148−153.

(45) Cortese, S.; Khiat, A.; Carta, D.; Light, M. E.; Prodromakis, T. An Amorphous Titanium Dioxide Metal Insulator Metal Selector Device for Resistive Random Access Memory Crossbar Arrays with Tunable Voltage Margin. *Appl. Phys. Lett.* **2016**, *108*, No. 033505.

(46) Lew, W. S.; Loy, D. J. J.; Dananjaya, P. A.; Chakrabarti, S.; Tan, K. H.; Chow, S. C. W.; Toh, E. H.; Lew, W. S. Oxygen Vacancy Density Dependence with a Hopping Conduction Mechanism in Multilevel Switching Behavior of HfO_2-Based Resistive Random Access Memory Devices. *ACS Appl. Electron. Mater.* **2020**, *2*, 3160−3170.

(47) Sharath, S. U.; Vogel, S.; Molina-Luna, L.; Hildebrandt, E.; Wenger, C.; Kurian, J.; Duerrschnabel, M.; Niermann, T.; Niu, G.; Calka, P.; Lehmann, M.; Kleebe, H.-J.; Schroeder, T.; Alff, L. Control of Switching Modes and Conductance Quantization in Oxygen Engineered HfO_x Based Memristive Devices. *Adv. Funct. Mater.* **2017**, *27*, No. 1700432.

(48) Milo, V.; Zambelli, C.; Olivo, P.; Pérez, E.; K Mahadevaiah, M.; G Ossorio, O.; Wenger, C.; Ielmini, D. Multilevel HfO_2-Based RRAM Devices for Low-Power Neuromorphic Networks. *APL Mater.* **2019**, *7*, No. 081120.

(49) Yu, S.; Chen, H.-Y.; Gao, B.; Kang, J.; Wong, H.-S. P. HfO_x-Based Vertical Resistive Switching Random Access Memory Suitable for Bit-Cost-Effective Three-Dimensional Cross-Point Architecture. *ACS Nano* **2013**, *7*, 2320−2325.

(50) Wang, C.; Wu, H.; Gao, B.; Wu, W.; Dai, L.; Li, X.; Qian, H. Ultrafast RESET Analysis of HfO_x-Based RRAM by Sub-Nanosecond Pulses. *Adv. Electron. Mater.* **2017**, *3*, No. 1700263.

(51) Yu, S. Neuro-Inspired Computing with Emerging Nonvolatile Memorys. *Proc. IEEE* **2018**, *106*, 260−285.

(52) Chen, P.-Y.; Lin, B.; Wang, I.; Hou, T.; Ye, J.; Vrudhula, S.; Seo, J.; Cao, Y.; Yu, S. In *Mitigating Effects of Non-Ideal Synaptic Device Characteristics for on-Chip Learning*, 2015 IEEE/ACM International Conference on Computer-Aided Design (ICCAD) 2015; pp 194−199.

(53) Lee, S.-H.; Yamasue, E.; Okumura, H.; Ishihara, K. N. Effect of Substrate Roughness and Working Pressure on Photocatalyst of N-Doped TiO_x Films Prepared by Reactive Sputtering with Air. *Appl. Surf. Sci.* **2015**, *324*, 339−348.

(54) Nandi, S. K.; Liu, X.; Venkatachalam, D. K.; Elliman, R. G. Effect of Electrode Roughness on Electroforming in HfO_2 and Defect-Induced Moderation of Electric-Field Enhancement. *Phys. Rev. Appl.* **2015**, *4*, 64010.

(55) Jeong, H. Y.; Kim, Y. I.; Lee, J. Y.; Choi, S.-Y. A Low-Temperature-Grown TiO_2-Based Device for the Flexible Stacked RRAM Application. *Nanotechnology* **2010**, *21*, No. 115203.

(56) Upadhyay, N. K.; Blum, T.; Maksymovych, P.; Lavrik, N. V.; Davila, N.; Katine, J. A.; Ievlev, A. V.; Chi, M.; Xia, Q.; Yang, J. J. Engineering Tunneling Selector to Achieve High Non-Linearity for 1S1R Integration. *Front. Nanotechnol.* **2021**, *3*, No. 656026.

https://doi.org/10.1021/acsami.2c11016
ACS Appl. Mater. Interfaces 2022, 14, 35959−35968